

# Single-, Double-, and Triple-Network Macroporous Rubbers as a Passive Sampler

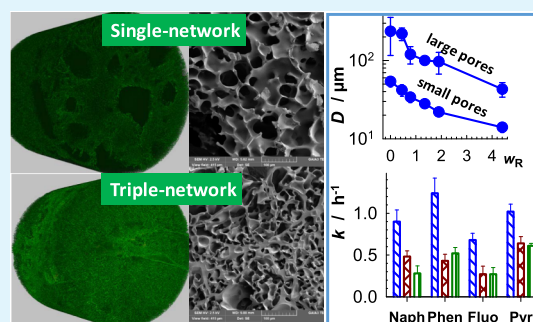
Berkant Yetiskin,<sup>†</sup> Oktay E. Tureyen,<sup>‡</sup> Atilla Yilmaz,<sup>‡</sup> Sevil D. Yakan,<sup>‡</sup> Oya S. Okay,<sup>\*,‡</sup> and Oguz Okay<sup>\*,†</sup>

<sup>†</sup>Department of Chemistry and <sup>‡</sup>Department Ocean Engineering, Istanbul Technical University, Maslak, 34469 Istanbul, Turkey

## Supporting Information

**ABSTRACT:** Over the past decades, large quantities of organic compounds including polycyclic aromatic hydrocarbons (PAHs) entering aquatic systems create acutely toxic effects and chronic abnormalities in aquatic organisms. Passive sampling is an effective technique to detect organic compounds at very low concentrations in water by accumulating them in their structure to a measurable concentration level. Polymeric passive samplers reported so far have a nonporous structure, and hence, the absorption of organic compounds into the passive sampler is governed by their slow diffusion process. We present here novel macroporous rubber sorbents as monophasic passive samplers with tunable pore morphologies, extraordinary mechanical properties, and high sorption rates and capacities for PAHs. Sorbent materials based on single-network (SN), double-network (DN), and triple-network (TN) butyl rubber were prepared via the cryogelation technique from butyl rubber solutions in benzene as the solvent at  $-18\text{ }^{\circ}\text{C}$  using a sulfur monochloride cross-linker. To obtain macroporous rubbers with DN and TN structures, the reactions were conducted in the macropores of SN and DN rubber networks, respectively. The porous morphology and the mechanical behavior of the rubbers can be tuned by adjusting the weight ratio  $w_R$  of the network components. The rubbers exhibit two generations of pores, namely, large and small pores with diameters  $40\text{--}240$  and  $14\text{--}54\text{ }\mu\text{m}$ , respectively. The sizes of both large and small pores decrease and approach each other as  $w_R$  is increased. Four PAH compounds, namely, naphthalene, phenanthrene, fluoranthene, and pyrene with two to four aromatic rings, dissolved in filtered seawater with a salinity of 22 ppt were used to highlight the correlations between the properties of macroporous rubbers and their absorption rates and capacities. Nonporous silicone rubber reported before as a passive sampler has the lowest absorption rate and capacity as compared to the macroporous rubbers. The SN rubber absorbs most rapidly PAHs because of its largest porosity, whereas the TN rubber with the smallest pores exhibits the highest sorption capacity.

**KEYWORDS:** butyl rubber, cryogels, macroporous, passive sampler, polycyclic aromatic hydrocarbons



## INTRODUCTION

In the past decades, large quantities of organic compounds entering aquatic systems create acutely toxic effects and chronic abnormalities in aquatic organisms. Although the dissolved concentration of organic compounds in aquatic systems is low because of their very low water solubilities, they are easily uptaken by the organisms, and hence, these pollutants move through the food chain with increasing level of biomagnification. It is thus a challenging task to detect their levels with sufficient selectivity and sensitivity. Passive sampling is an effective technique to detect organic compounds such as polycyclic aromatic hydrocarbons (PAHs) at very low concentrations in water by accumulating them in their structure to a measurable concentration level.<sup>1–6</sup> When compared to biomonitoring carried out with organisms, passive samplers are not affected by biological activities such as metabolism and excretion, which may alter the sampled amounts of the compounds of interest. Besides, passive samplers provide time-weighted average concentrations,

which are not affected by instantaneous pollutant inputs to the sampling site.

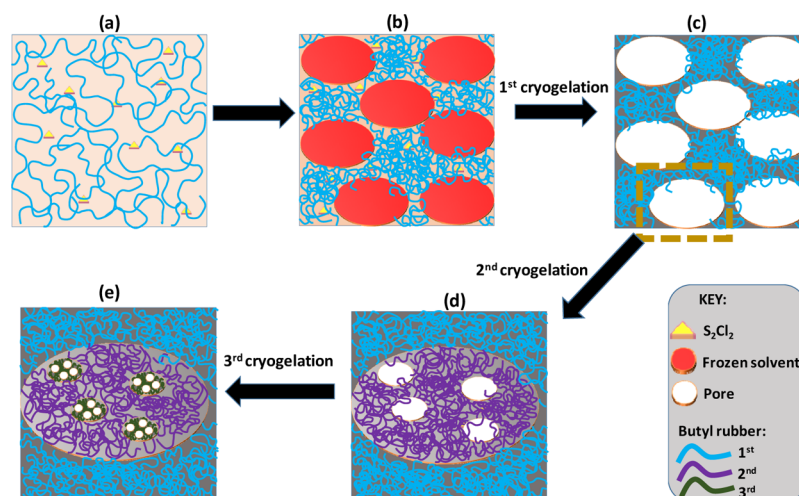
Biphasic passive samplers such as semipermeable membrane devices (SPMDs) consisting of polyethylene membranes filled with triolein have been widely used as a passive sampler to monitor organic chemicals.<sup>7</sup> Recent studies show that monophasic polymeric passive samplers such as polyoxymethylene, low-density polyethylene, and polydimethylsiloxane (PDMS) have several advantages over SPMDs as effective passive samplers in monitoring pollution level in aquatic systems.<sup>8</sup> To our knowledge, polymeric passive samplers developed so far have a nonporous structure, and hence, the diffusion of organic chemicals into the passive sampler determines the absorption process of organic chemicals. In contrast, for a passive sampler with interconnected pore

Received: May 21, 2019

Accepted: July 10, 2019

Published: July 10, 2019

Scheme 1. Cartoon Showing Formation of Single- (a–c), Double- (d), and Triple-Network Rubbers (e)



structure, organic chemicals are absorbed through its pores by convection which is faster than diffusion.<sup>9</sup>

Although several strategies have been developed to produce macroporous polymers,<sup>10–13</sup> cryogelation technique has several advantages because of the extraordinary properties of the resulting polymers such as high porosity, stable porous structure, sponge-like squeezability, and a high mechanical strength.<sup>14–17</sup> By this technique, the cross-linking reactions of linear polymers are conducted in aqueous or organic solutions below the freezing temperature, as schematically illustrated in Scheme 1a,b. As the solvent freezes, polymers and cross-linkers separated from the solvent crystals accumulate in still unfrozen regions of the cryogelation system, leading to the formation of a concentrated polymer solution, called cryoconcentration (Scheme 1b). After the thermal equilibrium is reached with the surroundings, the cryogelation system is composed of a highly concentrated solution phase and pure solvent crystals.<sup>15</sup> Generally, the effect of cryoconcentration is dominated over the reduction in cross-linking rates at low temperatures so that cross-linked polymers can be prepared even at very low concentrations of the polymer.<sup>15</sup> After completing the cryogelation reaction and melting the solvent crystals, a three-dimensional (3D) network structure with macropores is obtained (Scheme 1c).

Cryogelation reactions are mainly conducted in aqueous solutions to prepare macroporous hydrogels. Lozinsky et al. were the first to investigate the cryogelation reactions of polystyrene and *N*-vinylpyrrolidone–maleic anhydride copolymers in organic solutions in the presence of chemical cross-linkers.<sup>18</sup> They showed that the reactions conducted in dimethyl sulfoxide (DMSO) and nitrobenzene at subzero temperatures display similar characteristics as that in aqueous solutions.<sup>18</sup> Recently, hydrophobic cryogels based on acrylic and methacrylic monomers and PDMS were prepared in organic solvents including dioxane, cyclohexane, and DMSO.<sup>19–22</sup> Wong et al. presented cryogelation of acrylate-based monomer mixtures in DMSO to synthesize shape-memory polymer foams with tunable porous morphology and properties.<sup>22</sup> It was shown that the alignment of the pores and the porosity can be varied by changing the freezing rate and monomer concentration.

Butyl rubber (isobutylene-isoprene rubber, IIR) is a synthetic elastomer composed of isobutylene and 0.5–3 mol

% isoprene units serving as sites for covalent cross-linking of the rubber. Soft IIR can be converted into an elastic IIR by its cross-linking reactions, called vulcanization, usually conducted using sulfur or sulfur compounds as cross-linkers in the bulk phase.<sup>23</sup> We have shown that the vulcanization of several rubbers including IIR can be conducted in organic solutions using sulfur monochloride  $S_2Cl_2$  as a cross-linker via cryogelation technique to produce macroporous rubbers.<sup>24,25</sup> Benzene with a freezing temperature of 5.5 °C is generally used as the solvent, and cryogelation reactions are usually conducted 20–25 °C below this temperature.<sup>24,26</sup> High toughness, squeezability, hydrophobicity, and fast responsivity of macroporous rubbers expand the potential applications of IIR such as absorbent materials for the removal of oil spill from aquatic environments.<sup>27,28</sup> In our previous work,<sup>24</sup> we investigated the effects of various synthetic parameters including the temperature and the concentrations of the cross-linker  $S_2Cl_2$  and butyl rubber on the morphology of the cryogels. The average width and length of the pores were found to be  $40 \pm 12$  and  $58 \pm 17$   $\mu\text{m}$ , respectively, independent of the concentrations of rubber and  $S_2Cl_2$  as well as on the cryogelation temperature. However, the efficiency of macroporous IIR rubbers as a passive sampler for monitoring PAHs in the aquatic environment requires a tunable porous structure. Moreover, the existence of both large and small pores in a sorbent material is important because of the opposite effect of the pore size on the sorption rate and sorption capacity. Such a porous structure in rubber cryogels cannot be achieved using the one-step cryogelation reaction reported before.

We present here for the first time the fabrication of novel macroporous IIR rubbers with double-network (DN) and triple-network (TN) structures exhibiting a wide range of tunable pore structures and mechanical properties. The DN structure was generated by conducting the cryogelation reactions in the large pores of a single-network (SN) rubber, as illustrated in Scheme 1d. Thus, filling the pores of the SN rubber with a benzene solution of IIR and  $S_2Cl_2$  cross-linker followed by cryogelation leads to the formation of a second generation of pores within the large pores of the SN rubber. Repeating this step leads to the formation of a TN rubber containing a third generation of pores (Scheme 1e). As will be seen below, macroporous SN, DN, and TN rubbers with a tunable pore structure can successfully be prepared by

successive cryogelation reactions. We show that the mass ratio of the network components determines the morphology and mechanical properties of macroporous rubbers and their effectivity as passive samplers for monitoring PAHs in an aqueous environment.

## EXPERIMENTAL PART

**Materials.** Butyl rubber (IIR, 1675N, Togliatti, Russia) containing 1.5 mol % isoprene units was dissolved in toluene to remove the impurities and then precipitated in an excess of methanol, followed by drying under vacuum to constant weight. Sulfur monochloride ( $S_2Cl_2$ , Sigma-Aldrich), benzene (Merck), toluene, and methanol (both Tekkim, Turkey) were used without further purification. PDMS elastomer kSil GP60 as a reference passive sampler was purchased from Silicone Engineering Ltd. (Blackburn, UK). PAHs used in the sorption experiments, namely, naphthalene (Naph, Sigma-Aldrich), fluoranthene (Fluo, Fluka), pyrene (Pyr, Fluka), and phenanthrene (Phen, Fluka), were used as received.

**Preparation of Macroporous Rubbers.** Macroporous SN, DN, and TN butyl rubbers (IIR) were prepared in benzene solutions of IIR using  $S_2Cl_2$  as a cross-linker.  $S_2Cl_2$  concentration and the cryogelation temperature were fixed at 6 v/w % (with respect to IIR) and  $-18\text{ }^\circ\text{C}$ , respectively, which were the optimum conditions for the cryogelation of several rubbers with a SN structure.<sup>24,28</sup> The SN rubber was prepared at an IIR concentration ( $C_1$ ) of 5 w/v %. Briefly, IIR (5 g) was dissolved in benzene (100 mL) in a glass beaker at  $23 \pm 2\text{ }^\circ\text{C}$  overnight to obtain a homogeneous solution. After addition of  $S_2Cl_2$  (0.30 mL) and stirring for 2 min, the solution was transferred into 5 mL plastic syringes of 14 mm in diameter and Petri dishes of 10 cm in diameter and 13 mm in height. Finally, the syringes and sealed Petri dishes were immersed in a deep freezer at  $-18\text{ }^\circ\text{C}$ , and the reactions were conducted for 24 h. In this way, macroporous SN rubber specimens in the form of cylinders of around 14 mm in diameter and rubber sheets of about 3 mm in thickness were obtained. Macroporous SN rubbers were then extracted in toluene and finally dried to constant mass, as described in the next section.

DN rubbers were synthesized by swelling dried SN rubber in benzene solution of IIR at various concentrations ( $C_2$ ) between 2.5 and 10 w/v % containing a  $S_2Cl_2$  cross-linker. Typically, dried SN rubber specimens in the form of cylinders of 1 cm in length and sheets of around 3 mm in thickness were immersed in 100 mL of benzene solution containing IIR (2.5 to 10 g) and  $S_2Cl_2$  (6 v/w % with respect to IIR). After attaining swelling equilibrium which required 5–10 min, swollen rubber specimens in the form of cylinders and sheets were sealed in 10 mL plastic syringes and closed Petri dishes. They were then placed in a deep freezer at  $-18\text{ }^\circ\text{C}$ , and cryogelation reactions were conducted for 24 h. TN rubbers were prepared as described above by immersing dried DN rubber prepared at  $C_2 = 10$  w/v % in benzene solution of IIR at a concentration ( $C_3$ ) of 10 w/v % containing 6 v/w %  $S_2Cl_2$ . The mass ratio of the network components with respect to the first single network,  $w_R$ , was calculated as

$$w_R = w_{2/1} + C_3(q_{w,2} - 1)(1 + w_{2/1}) \quad (1)$$

where  $w_{2/1}$  is the ratio of the second to the first network, that is,  $w_{2/1} = (q_{w,1} - 1)C_2$ ,  $q_{w,1}$  and  $q_{w,2}$  are the equilibrium weight swelling ratios (swollen mass/dry mass) of the SN and DN rubbers, respectively, in benzene solution of IIR and  $S_2Cl_2$ . The rubber concentration  $C_{IIR}$  just after cryogelation in benzene was 5.7 wt % for the SN rubber, whereas for DN and TN rubbers,  $C_{IIR}$  was calculated using the equations

$$C_{IIR} \text{ wt \%} = \frac{(1 + w_{2/1})}{q_{w,1}} \times 10^2 \quad (2a)$$

$$C_{IIR} \text{ wt \%} = \frac{1 + (q_{w,2} - 1)C_3}{q_{w,2}} \times 10^2 \quad (2b)$$

respectively. Synthesis conditions of macroporous SN, DN, and TN rubbers are compiled in Table 1.

**Table 1.** Preparation Condition of SN, DN, and TN Rubbers<sup>a</sup>

code	$C_1$ w/v %	$C_2$ w/v %	$C_3$ w/v %	$q_{w,1}$	$q_{w,2}$	$w_R$	$C_{IIR}$ wt %
SN	5.0	0	0	22 (3)		0	5.7
DN	5.0	2.5	0	19 (1)		0.45 (0.03)	7.6 (0.3)
DN	5.0	5.0	0	18 (1)		0.85 (0.05)	10.3 (0.3)
DN	5.0	7.5	0	19 (1)		1.35 (0.08)	12.4 (0.4)
DN	5.0	10	0	20 (2)		1.9 (0.2)	14.5 (1)
TN	5.0	10	10	20 (2)	10 (3)	4.5 (0.4)	19 (2)

<sup>a</sup>Standard deviations are in parenthesis.

**Characterization of Macroporous Rubbers.** Swelling and gel fraction measurements were performed by immersing cross-linked rubber specimens of about 1 cm in length in an excess of toluene, a good solvent for IIR, at  $23 \pm 2\text{ }^\circ\text{C}$  for at least 1 week to remove soluble species. To eliminate the solvent effect on the microstructure of the rubbers, toluene in the specimens was then replaced with the poor solvent methanol and finally dried to constant mass under vacuum. The gel fraction  $W_g$  defined as the mass of toluene-insoluble IIR prepared from 1 g of linear IIR was calculated using the equation

$$W_g = \frac{m_{dry}}{m_o C_{IIR}} \quad (3)$$

where  $m_{dry}$  and  $m_o$  are the masses of the rubber samples in dry state and after preparation, respectively. The equilibrium weight and volume swelling ratios of the rubbers in toluene, represented by  $q_w$  and  $q_v$ , respectively, were calculated as

$$q_w = \frac{m_s}{m_{dry}} \quad (4a)$$

$$q_v = \left( \frac{D_s}{D_{dry}} \right)^3 \quad (4b)$$

where  $m_s$  and  $D_s$  are the mass and the diameter of swollen rubber specimens, respectively, and  $D_{dry}$  is the diameter of the dry rubber specimen. The total volume of the pores  $V_p$  in the rubbers was calculated from methanol uptake capacity because it is a poor solvent for IIR and hence preferentially enters the open pores. To determine  $V_p$ , rubber specimens in the dry state were placed in excess amount of methanol, and the mass  $m_M$  of the specimens was measured.  $V_p$ , the total pore volume per unit mass of the rubber, was estimated by

$$V_p = \frac{m_M - m_{dry}}{d_M m_{dry}} \quad (5)$$

where  $d_M$  is methanol density ( $0.792\text{ g mL}^{-1}$ ).

The morphology of macroporous rubbers was investigated using scanning electron microscopy (SEM) and micro-computed tomography ( $\mu$ -CT). SEM images of the samples were recorded on a Tescan GAIA 3 field emission scanning electron microscope after sputter-coating with gold palladium on a Leica ACE 600 high vacuum sputter coater. The average diameter  $D$  of the pores was calculated by analyzing at least 10 SEM images of various magnifications using ImageJ software (NIH, USA).  $\mu$ -CT scanning was conducted on a  $\mu$ -CT Skyscan 1272 (Bruker, Belgium) without a filter and using the following parameters:  $15.3\text{ }\mu\text{m}$  pixel resolution, 55 kV voltage, 60  $\mu\text{A}$  current,  $180^\circ$  rotation around vertical axes, 70 ms integration time. The details of the measurements and the treatment of data were reported before.<sup>29</sup>

Mechanical measurements were conducted using a Zwick Roell instrument with a 500 N load cell. All the tests were carried out at 23

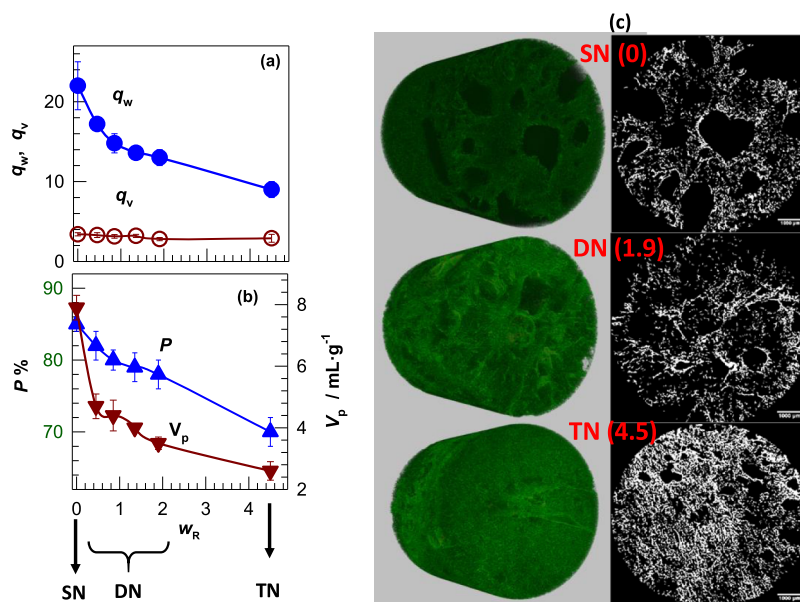


**Figure 1.** (a,b) Equilibrium weight  $q_w$  (filled circles) and volume swelling ratios  $q_v$  (open circles), the total porosity  $P$  (triangles up), and pore volume  $V_p$  (triangles down) of macroporous rubbers plotted against  $w_R$  ratio. (c) 3D (left) and 2D  $\mu$ -CT images (right) of SN, DN, and TN rubbers formed at  $w_R$  ratios shown in the parenthesis. Scale bars are 1 mm.

$\pm 2$  °C and at a strain rate of  $5 \text{ min}^{-1}$ . The nominal stress  $\sigma_{\text{nom}}$ , the force per cross-sectional area of the undeformed specimen, and the fractional deformation  $\varepsilon$  were recorded. Tensile tests were conducted on the rubber specimens in the form of sheets of about 10 mm in length and 2 mm in thickness. Young's modulus  $E$  of the rubber was calculated from the slope of  $\sigma_{\text{nom}}-\varepsilon$  curves between 5 and 15% elongation. Cylindrical rubber specimens of 14 mm in diameter and 3 mm in thickness were subjected to uniaxial compression tests, as detailed before.<sup>30</sup> To demonstrate the self-recoverability of the rubbers, successive compression cycles were conducted by first compressing the rubber specimens to a maximum strain of 80%, followed by unloading to zero strain at the same rate. After a waiting time of 1 min, these loading and unloading steps were repeated 9 times.

**Sorption Tests.** Macroporous rubbers and PDMS as a reference material were used for the sorption experiments of naphthalene (Naph), phenanthrene (Phen), fluoranthene (Fluo), and pyrene (Pyr) from aqueous solutions at  $23 \pm 1$  °C. The experiments were carried out by immersing rubber specimens, each 0.100 g, in 40 mL of aqueous PAH solutions prepared in filtered clean seawater with a salinity of 22 ppt. The PAH concentrations used in the experiments were selected by considering the solubility limits of the PAH compounds. In the first phase of the experiments, the concentration of PAH in the solution was monitored up to 12 h to highlight the initial uptake rate of the passive samplers. In the second phase, cumulative PAH concentration in the passive samplers was monitored over 30–40 days by refreshing PAH solution every day. The PAH concentration in the solution was determined by taking subsamples at predetermined time intervals and measuring the concentrations against the standards using a fluorescence spectrophotometer (PerkinElmer, LS-55).

## RESULTS AND DISCUSSION

**Macroporous Structure of a Cross-Linked Butyl Rubber.** Macroporous cross-linked rubber with a SN structure was prepared from the benzene solution of 5 w/v % butyl rubber (IIR) at  $-18$  °C in the presence of sulfur monochloride ( $\text{S}_2\text{Cl}_2$ ) as a cross-linker.<sup>24</sup> The filling of the pores in the SN rubber with a second benzene solution of IIR at various concentrations and  $\text{S}_2\text{Cl}_2$  followed by cryogelation at  $-18$  °C resulted in DN rubbers. By increasing the IIR concentration in

the second benzene solution from 2.5 to 10 w/v %, we were able to increase the weight ratio  $w_R$  of the second-to-first network components in the DN rubber up to 1.9 (Table 1). As will be seen below, increasing the weight ratio  $w_R$  significantly improves the mechanical properties of the rubbers. However, this ratio could not be further increased because the second benzene solution containing more than 10 wt % IIR was too viscous hindering its diffusion into the SN rubber. Therefore, we introduced the triple-networking strategy to further increase the weight ratio  $w_R$  of the network components. Thus, the pore filling of the DN rubber formed at  $w_R = 1.9$  with a third benzene solution of 10 wt % IIR and  $\text{S}_2\text{Cl}_2$  followed by cryogelation resulted in TN rubbers with a weight ratio  $w_R$  of the network components of 4.5. The measurement of the gel fractions  $W_g$  revealed that all rubbers exhibit a  $W_g$  value of around unity, indicating that the linear IIR was completely incorporated into the rubber network, that is, the vulcanization of IIR at  $-18$  °C was complete (Table S1).

Figure 1a shows the equilibrium weight  $q_w$  (filled symbols) and volume swelling ratios  $q_v$  (open symbols) of the rubbers in toluene, a good solvent for IIR, plotted as a function of the ratio of the network components  $w_R$ . SN rubber with  $w_R = 0$  exhibits a large weight swelling ratio  $q_w$  of  $22 \pm 3$ , whereas increasing  $w_R$  by introducing the second and third network components into the SN decreases  $q_w$  continuously and becomes  $9 \pm 1$  at the highest  $w_R$  ratio of 4.5. In contrast, the volume swelling degree  $q_v$  is  $w_R$ -independent and remains at  $3.1 \pm 0.2$ . Because volume swelling of a cross-linked porous rubber in a good solvent leads to the expansion of the polymer network because of the attractive polymer–solvent interactions, whereas its swelling ratio by weight additionally includes pore filling with the solvent, one may estimate the total open porosity  $P$  from the difference between  $q_w$  and  $q_v$  by<sup>9</sup>

$$P \% = \left( 1 - \frac{q_v}{1 + (q_w - 1)d_2/d_1} \right) \times 10^2 \quad (6)$$

where  $d_1$  and  $d_2$  are the densities of toluene ( $0.867 \text{ g mL}^{-1}$ ) and IIR ( $0.92 \text{ g mL}^{-1}$ ), respectively.

Figure 1b shows the porosity  $P$  calculated using eq 6, and the total pore volume  $V_p$  calculated from the uptake of the poor solvent methanol plotted against the ratio of the network components  $w_R$ . The porosity and the total pore volume decrease from 85 to 70% and from 7.9 to  $2.6 \text{ mL}\cdot\text{g}^{-1}$ , respectively, as  $w_R$  is increased from 0 to 4.5. Thus, the higher the  $w_R$  ratio, the lower is the porosity, indicating partial filling of the pores in SN and DN rubbers with the second and third network components, respectively. The results also reveal a significant effect of double- and triple-networking on the porosity of the rubbers.

To visualize the porous structure of the rubbers, SEM and  $\mu$ -CT techniques were used where the former provides a greater magnification and more accurate measurement of the pore sizes than  $\mu$ -CT.  $\mu$ -CT measurements were conducted on rubber specimens in the family tree starting with SN, going through DN with  $w_R = 1.9$  to the TN with  $w_R = 4.5$ . Figure 1c shows typical two-dimensional (2D) and 3D  $\mu$ -CT images of SN, DN, and TN rubbers formed at  $w_R = 0, 1.9$ , and 4.5, respectively (scale bars = 1 mm). The SN rubber has, in addition to micrometer-sized pores, millimeter-sized very large pores (large black areas in the image), which decrease in size and finally disappear after its double- and triple-networking. The size distributions of the pores in SN, DN, and TN rubbers given in Figure 2a support this finding; the volume fraction of

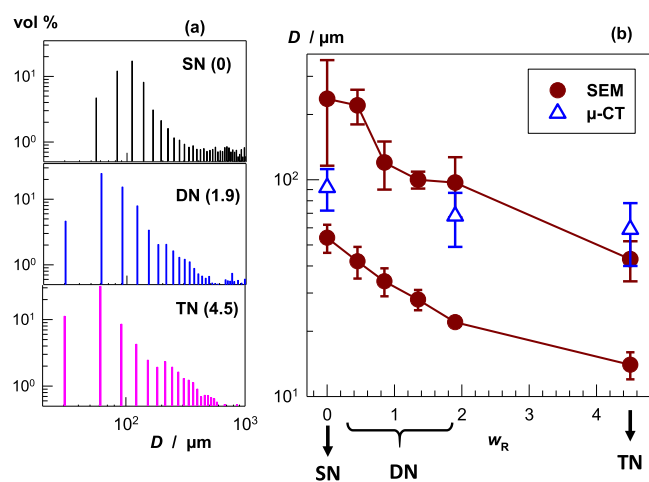


**Figure 2.** (a) Pore size distributions estimated from  $\mu$ -CT analysis of SN, DN, and TN rubbers with  $w_R$  ratios shown in the parenthesis. (b) Average pore diameters  $D$  of rubbers from  $\mu$ -CT (open triangles) and SEM analysis (filled circles) plotted against  $w_R$ .

millimeter-sized pores decreases after double- and triple-networking and a new generation of pores appears at around  $30 \mu\text{m}$ . For instance, the volume fractions of the pores between 13 and  $45 \mu\text{m}$  are 0.2, 5, and 11% for SN, DN, and TN with  $w_R = 0, 1.9$ , and 4.5, respectively. The total porosities estimated from  $\mu$ -CT analysis are 95, 84, and 74% for SN, DN, and TN, respectively, and hence show a similar trend as estimated from the swelling ratios using eq 6 and pore volume measurements (Figure 1b). Moreover,  $\mu$ -CT results also reveal that there are no closed pores in all rubbers, which is an important requirement for their applications in absorption processes. The thicknesses of the pore walls are  $30 \pm 7$ ,  $39 \pm 15$ , and  $44$

$\pm 16 \mu\text{m}$  for SN, DN, and TN rubbers, respectively, that is, it increases with increasing number of the network components.

Figure 3 shows SEM images of SN, DN, and TN rubbers with various  $w_R$  ratios as indicated. The structure consists of

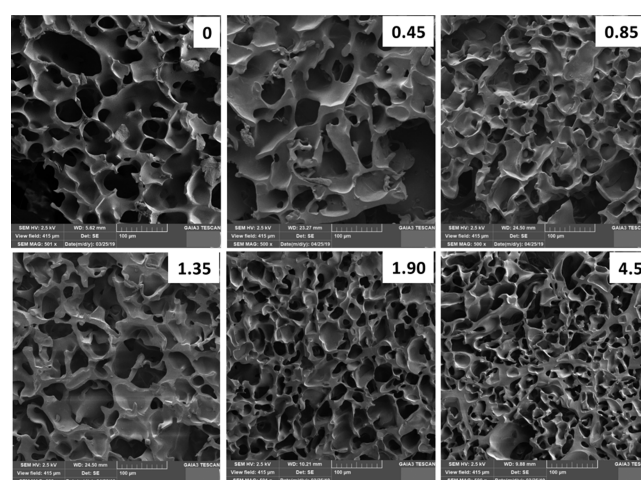


**Figure 3.** SEM images of macroporous SN, DN, and TN rubbers formed at various  $w_R$  ratios indicated. Scale bars are  $100 \mu\text{m}$ .

micrometer-sized irregular pores whose average size decreases while the pore walls become thicker as the  $w_R$  ratio is increased. Filled circles in Figure 2b show the average pore diameters  $D$  estimated by analyzing SEM images plotted against  $w_R$  ratio. We observed two generations of pores in all rubbers, namely, large and small pores with diameters 40–240 and  $14$ – $54 \mu\text{m}$ , respectively. The average diameters of both large and small pores decrease, and they approach each other as  $w_R$  is increased. For instance, in the family tree starting with SN through DN to the TN with  $w_R = 0, 1.9$ , and 4.5, respectively, the average diameter  $D$  of the large pores decreases from  $236 \pm 120$  through  $97 \pm 30$  to  $43 \pm 9 \mu\text{m}$ , revealing filling of the large pores in SN with the second and third network components and formation of more mono-disperse pores. Small pores in the rubbers show a similar trend and  $D$  first decreases from  $54 \pm 8$  to  $22 \pm 1 \mu\text{m}$  and then to  $14 \pm 2 \mu\text{m}$  after double- and triple-networking, respectively.

We have to mention that the large polydispersity of the pores in SN rubber is due to the coexistence of two mechanisms for the formation of pores during cryogelation.<sup>31</sup> The first mechanism is the presence of solvent crystals acting as a template for the formation of micrometer-sized pores. The second is the macro-phase separation of IIR at low temperature at which benzene becomes a poor solvent for IIR, which leads to the formation of micrometer- to millimeter-sized pores.<sup>31</sup> The appearance of more regular pores in both DN and TN reflects the filling of large pores with the second and third network components. Open symbols in Figure 2b representing the  $w_R$  ratio dependence of the pore diameters less than  $150 \mu\text{m}$  estimated by CT gives a similar trend with the SEM results but slightly larger diameters. We have to mention that the  $\mu$ -CT technique calculates the pore sizes from the number of pixels in the pores. Because the pixel resolution is  $15 \mu\text{m}$ ,  $\mu$ -CT estimates the pore sizes at least  $15 \mu\text{m}$  higher as compared to SEM, which is also reflected in higher total porosities.

**Mechanical Properties.** The mechanical properties of the rubbers were determined by uniaxial elongation and compression tests at  $23 \pm 2 \text{ }^\circ\text{C}$ . The measurements revealed

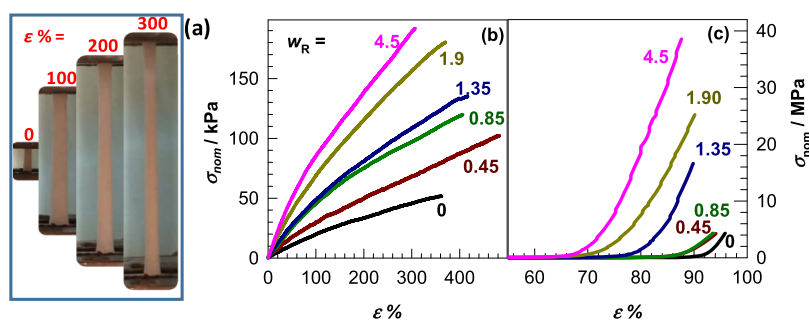


**Figure 4.** (a) Images of a TN rubber specimen during the elongation tests. (b,c) Typical tensile (b) and compressive nominal stress ( $\sigma_{\text{nom}}$ )–strain ( $\epsilon$ ) curves of the rubbers (c). The mass ratios  $w_R$  of the network components are indicated.

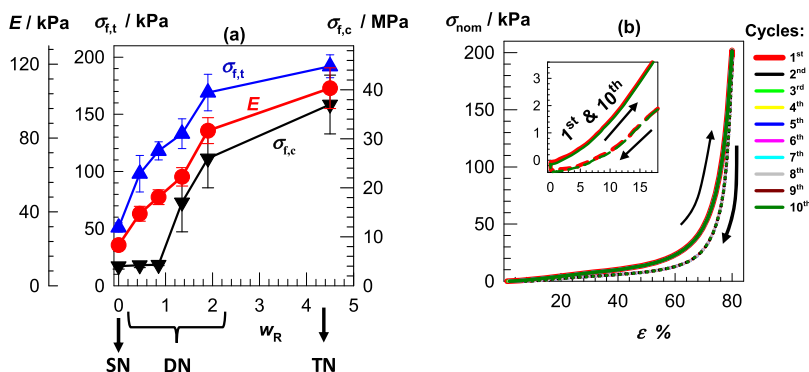


**Figure 5.** (a) Modulus  $E$ , tensile  $\sigma_{f,t}$ , and compressive fracture stresses  $\sigma_{f,c}$  of the rubbers shown as a function of the  $w_R$  ratio. (b) Ten successive loading and unloading cycles conducted on a TN rubber specimen. The loading and unloading curves are shown by solid and dotted curves, respectively. The inset is a zoom-in to the first and last cycles between 0 and 18% strains.

reversible deformation and high stretchability of all rubbers. For instance, the images in Figure 4a present a TN rubber specimen during stretching up to 300%. After stretching and unloading, the specimen recovers its initial length without any permanent deformation. Figure 4b,c shows tensile and compressive stress–strain curves of the rubbers with various  $w_R$ , respectively. All rubbers sustain 300–500% elongation ratios and 50–190 kPa tensile stresses. Young's modulus  $E$ , the tensile  $\sigma_{f,t}$ , and compressive fracture stresses  $\sigma_{f,c}$  of the rubbers are shown in Figure 5a as a function of the weight ratio  $w_R$  of the network components. The mechanical performance of the rubbers significantly improves with increasing  $w_R$  ratio of the network components. For instance, the modulus  $E$  and compressive fracture stress  $\sigma_{f,c}$  increase by 5 and 9 folds, respectively, as  $w_R$  is increased from 0 to 4.5. TN rubbers prepared at the highest  $w_R$  ratio have the highest modulus  $E$  ( $0.11 \pm 0.01$  MPa) and can sustain 0.19 and  $37 \pm 6$  MPa tensile and compressive stresses, respectively.

To determine the fatigue resistance of the rubbers against deformation, cyclic compression tests at a constant strain rate of  $5 \text{ min}^{-1}$  were performed by loading the samples up to 80% strain and then unloading. This loading and unloading cycle was repeated 9 times with a waiting time of 1 min between the cycles. The results are shown in Figure 5b for a TN rubber specimen where the loading and unloading curves are shown by the solid and dotted curves, respectively. Each loading or unloading curve exactly follows the previous one revealing reversibility of the cycles and self-recoverability of the rubber. This behavior is also illustrated in the inset to the figure, which is a zoom-in to the first and last cycles between 0 and 18% strains. Indeed, the hysteresis energy  $U_{\text{hys}}$ , that is, the area between the loading and unloading curves, is independent on

the number of cycles and remains at  $6.07 \pm 0.05 \text{ kJ}\cdot\text{m}^{-3}$ . Because  $U_{\text{hys}}$  corresponds to the energy dissipated due to the damage in the microstructure,<sup>32</sup> this reveals recovery of the original microstructure after the waiting time of 1 min. Thus, owing to the self-recovery ability of the rubbers, they have a high fatigue resistance against repeated deformations.

**Sorption of PAHs.** SN, DN, and TN rubbers with  $w_R$  ratios of 0, 1.9, and 4.5, respectively, with different porosities (85–70%), pore volumes ( $7.9\text{--}2.6 \text{ mL}\cdot\text{g}^{-1}$ ), and pore sizes and size distributions were selected for the sorption experiments together with nonporous PDMS as the reference material. Sorption experiments were carried out using four PAHs, namely, phenanthrene (Phen), naphthalene (Naph), pyrene (Pyr), and fluoranthene (Fluo), whose structures are shown in Scheme 2 together with their solubility parameters  $\delta$ , molar volumes  $V_m$ , and water solubilities  $s$  at 25 °C. The PAH

**Scheme 2. Structure, Solubility Parameter  $\delta$ , Molar Volume  $V_m$ , and Water Solubility  $s$  at 25 °C of Naphthalene (Naph), Phenanthrene (Phen), Fluoranthene (Fluo), and Pyrene (Pyr)**

	Naph	Phen	Fluo	Pyr
$\delta / \text{MPa}^{0.5}$	20.5	21.8	22.0	23.3
$V_m / \text{mL}\cdot\text{mol}^{-1}$	126	159	175	160
$s / \mu\text{g}\cdot\text{L}^{-1}$	31600	1150	265	134

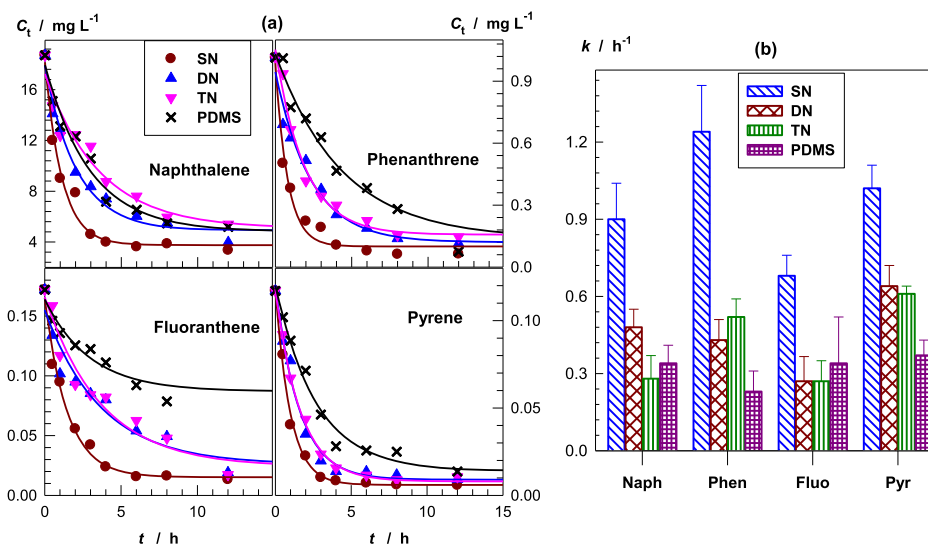


**Figure 6.** (a) Experimental data during the first 12 h of the sorption tests (symbols) and the results of curve fitting using eq 8 (curves). (b) Rate constant  $k$  of the sorption process as a function of the types of rubbers and PAHs.

compounds have two to four aromatic rings and exhibit solubility parameters between 20.5 and 23.3  $\text{MPa}^{0.5}$ , which are closer to IIR than PDMS (16.8 vs 14.9  $\text{MPa}^{0.5}$ ), revealing that these PAHs would have stronger interactions with IIR than PDMS. Two sets of sorption experiments were conducted by placing the rubber specimens in aqueous solutions of PAHs in filtered seawater with a salinity of 22 ppt. In the first set, the concentration of PAH in the solution was monitored up to 12 h to highlight the initial uptake rate of the rubbers. In the second set, cumulative PAH concentration in the rubber specimens was monitored over 30–40 days by refreshing PAH solutions every day.

Figure 6a shows the variations of the concentrations  $C_t$  of Naph, Phen, Fluo, and Pyr as a function of the contact time  $t$  during the first 12 h of sorption experiments. The SN rubber most rapidly absorbs all the PAHs studied from the solution and the total absorbed amount of each PAH is the highest as compared to other rubbers, which is attributed to its largest porosity and pore volume. If we assume that the decay of PAH concentration with time follows a first-order kinetics, the sorption process by the macroporous rubbers can be written as<sup>33,34</sup>

$$\frac{dq_t}{dt} = k(q_e - q_t) \quad (7)$$

where  $q_e$  and  $q_t$  represent the PAH amounts absorbed at equilibrium and time  $t$ , respectively, and  $k$  is the rate constant. Solution of eq 7 gives

$$C_t = C_0 - C_{\text{eq}}(1 - e^{-kt}) \quad (8)$$

where  $C_0$ ,  $C_t$ , and  $C_{\text{eq}}$  are PAH concentrations in the solution at time zero, time  $t$ , and equilibrium, respectively. The results of curve fitting using eq 8 for four different PAHs are shown in Figure 6a by the curves. A good agreement between the experimental and predicted values of eq 8 is seen from the figures. We have to mention that a second-order kinetics in the form of  $dq_t/dt = k'(q_e - q_t)^2$  results in a similar fit to the experimental data (Figure S1). The rate constants  $k$  extracted from the first-order fits are compiled in Figure 6b for four PAHs and four rubbers. SN exhibits the highest rate constant  $k$

for all PAHs. The average  $k$  values for all PAHs are  $1.0 \pm 0.2$ ,  $0.46 \pm 0.15$ ,  $0.42 \pm 0.06$ , and  $0.32 \pm 0.06$  for SN, DN, TN, and PDMS, respectively, that is, it decreases in the order SN > DN > TN > PDMS. Thus, the larger the total volume of the pores, the faster is the rate of absorption of PAHs from aqueous solutions.

Results of longtime experiments up to 30–40 days are shown in Figure 7a–d where the absorbed amount of Naph,

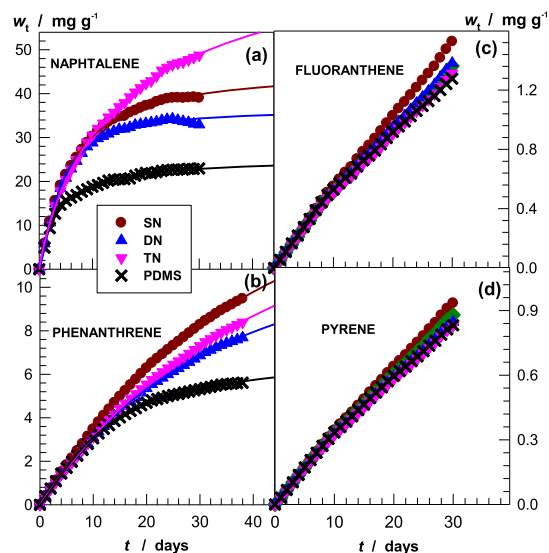


**Figure 7.** Absorbed amount of Naph (a), Phen (b), Fluo (c), and Pyr (d) by 1 g of rubber sorbent ( $w_t$ ) plotted against the contact time  $t$ . Experimental data are represented by symbols, while the curves in (a,b) are the results of curve fitting using eq 7.

Phen, Fluo, and Pyr, respectively, by 1 g of rubber ( $w_t$ ) is plotted against the contact time  $t$ . Because of very low water solubilities of Fluo and Pyr (Scheme 2), their experimental  $w_t$  versus time data were still in the initial linear regime after 30 days of monitoring so that their saturated concentrations cannot be estimated. Long-term data obtained from the solutions of Naph and Phen could be well fitted to the modified Hill equation<sup>35–39</sup>

$$w_t = w_{\text{eq}} \frac{t^n}{t^n + t_{1/2}^n} \quad (9)$$

where  $w_{\text{eq}}$  is the absorbed amount of PAH at equilibrium, that is, at the final steady-state PAH concentration,  $t_{1/2}$  is the half-equilibrium time at which  $w_t = w_{\text{eq}}/2$ , and the exponent  $n$  was found to be independent on the types of rubbers and PAHs and equals to  $1.1 \pm 0.2$ . The curves in Figure 7a,b showing the results of curve fitting reveal that eq 9 can be used to quantitatively characterize the sorption kinetics of PAHs. Such perfect modeling the shape of the time-dependent PAH concentration variations is of prime importance in predicting the long-term properties of passive samplers. To the best of our knowledge, eq 9 has not been used in such applications.

Figure 8 presents the amount of Naph and Phen absorbed at equilibrium  $w_{\text{eq}}$  together with the half-equilibrium time  $t_{1/2}$  as a

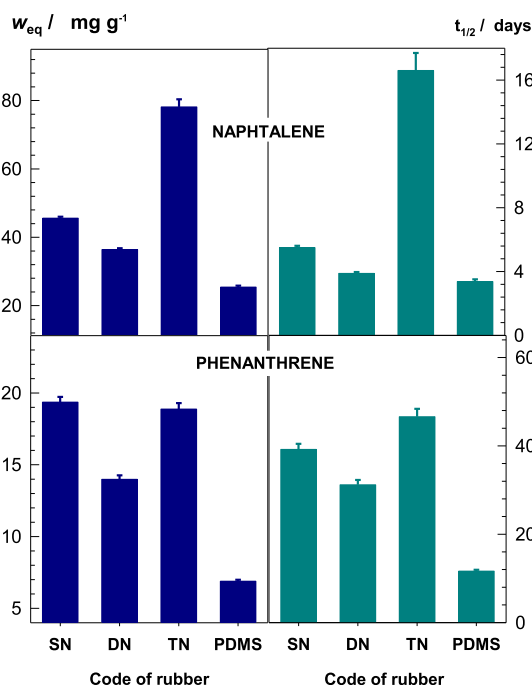


**Figure 8.** Sorbed amount of PAH at equilibrium  $w_{\text{eq}}$  and the half-equilibrium time  $t_{1/2}$  as a function of the types of sorbents and PAHs.

function of the types of rubbers and PAHs. PDMS with a nonporous structure exhibits the lowest absorption capacity for both Naph and Phen. This highlights the importance of a macroporous structure for materials to be used as passive samplers. Moreover, the TN sorbent with the smallest pores and porosity among the macroporous rubbers absorbs the highest amount of Naph. Thus, although the initial sorption rate of TN for PAHs is slow, it is capable of absorbing a large amount of Naph from aqueous solutions. This interesting finding can be attributed to the opposite effect of the pore size on the sorption rate and sorption capacity. Although a large pore size and a high porosity of around 90% provide rapid sorption of PAHs at short times as observed by the SN rubber, at longer contact times, PAHs located in the large pores can easily diffuse out of the rubber phase because of their large water contents. This finding shows a significant effect of the pore morphology of passive samplers in their efficiency in short- and long-time field applications. We have to note that the lower absorption capacity of DN as compared to that of

SN can be attributed to its smaller pore volume ( $3.5$  vs  $7.9 \text{ mL} \cdot \text{g}^{-1}$ ) and lower volume fraction of its pores between  $13$  and  $45 \mu\text{m}$  as compared to TN ( $5$  vs  $11\%$ ).

Figure 8 also shows that the half-equilibrium time  $t_{1/2}$  of TN in Naph solution is  $17 \pm 1$  days, which is 3- to 5-fold longer than the other sorbents. This means that the TN sorbent can be used for long-time monitoring of PAHs in aquatic systems. Moreover, when the sorption tests are conducted with Phen instead of Naph, the absorption capacity of SN approaches to that of TN (Figure 8). This behavior is attributed to 30-times lower water solubility of Phen as compared to that of Naph, which provides its accumulation in the hydrophobic sorbent phase instead of water (Scheme 2). We have to note that the PAH compounds used in the absorption tests have solubility parameters  $\delta$  between  $20.5$  and  $23.3 \text{ MPa}^{0.5}$  as compared to  $\delta = 16.8 \text{ MPa}^{0.5}$  reported for IIR.<sup>25</sup> Thus, rubber sorbents with  $\delta$  values closer to PAHs than IIR such as *cis*-polybutadiene and styrene-butadiene rubber with  $\delta = 18.0$  and  $18.1 \text{ MPa}^{0.5}$ , respectively,<sup>40</sup> would have a higher sorption capacity for PAHs as compared to that for the IIR sorbent.

## CONCLUSIONS

Passive sampling is an efficient technique for monitoring the dissolved concentration of PAHs in aquatic systems. We presented here a series of novel macroporous rubber sorbents as single-phase passive samplers with tunable pore morphologies, extraordinary mechanical properties, and high sorption rates and capacities for PAHs. Sorbent materials based on SN, DN, and TN butyl rubber were prepared via cryogelation technique from butyl rubber solutions in benzene as the solvent at  $-18 \text{ }^\circ\text{C}$  using a  $\text{S}_2\text{Cl}_2$  cross-linker. To obtain rubber sorbents with DN and TN structures, cryogelation reactions were conducted within the pores of SN and DN rubber networks, respectively. The porosity, average pore diameter, and mechanical properties including the modulus and fracture stress could be tuned by adjusting the weight ratio  $w_{\text{R}}$  of the network components. Increasing  $w_{\text{R}}$  ratio decreases both the average pore diameter and the total porosity of the rubbers, whereas their mechanical properties significantly increase. Four PAH compounds, namely, Naph, Phen, Fluo, and Pyr, with two to four aromatic rings were used to highlight the relations between the properties of macroporous rubber sorbents and their absorption rates and capacities for the PAHs. It was shown that the nonporous PDMS rubber reported before as a passive sampler has the lowest absorption rate and absorption capacity as compared to macroporous rubber sorbents presented here. The SN rubber sorbent absorbs most rapidly PAHs which are attributed to its largest porosity and pore volume. Moreover, the TN sorbent has the highest sorption capacity because of its smaller pores and low porosity, preventing the escape of PAHs from the sorbent to the solution phase. The present experimental studies with PAHs highlight the potential use of SN and TN monophasic macroporous rubber sorbents in monitoring studies of surface waters. However, we should note that it is necessary to determine the sorbent-water partition coefficients and in situ sampling rates. The rubber sorbents should also be tested in the field to see the spectrum of the substances accumulated in and compared with those used widely as passive samplers. The deployment protocols of the rubber sorbents to the monitoring sites should also be clearly defined.

## ■ ASSOCIATED CONTENT

### ■ Supporting Information

The Supporting Information is available free of charge on the ACS Publications website at DOI: 10.1021/acsami.9b08788.

Gel fractions and the second-order fit results of the sorption data (PDF)

## ■ AUTHOR INFORMATION

### Corresponding Authors

\*E-mail: oya.okay@itu.edu.tr (O.S.O.).

\*E-mail: okayo@itu.edu.tr (O.O.).

### ORCID

Oguz Okay: 0000-0003-2717-4150

### Author Contributions

The manuscript was written through contributions of all authors. All authors have given approval to the final version of the manuscript.

### Notes

The authors declare no competing financial interest.

## ■ ACKNOWLEDGMENTS

This research was funded by the Scientific and Technical Research Council of Turkey (TUBITAK), CAYDAG, 117Y099. O.O. thanks the Turkish Academy of Sciences (TUBA) for the partial support.

## ■ REFERENCES

- (1) EU Technical Guidance Document 19. *Common Implementation Strategy for the Water Framework Directive (2000/60/EC). Guidance on Surface Water Chemical Monitoring under the Water Framework Directive. Technical Report*, 2009; Vol. 025, pp 10–37.
- (2) EU-Directive 2013/39/EU of the European Parliament and of the Council Amending Directives 2000/60/EC and 2008/105/EC as Regards Priority Substances in the Field of Water Policy. *Off. J. Eur. Union* **2013**, L226, 1–17.
- (3) Gonzalez-Rey, M.; Tapie, N.; Le Menach, K.; Dévier, M.-H.; Budzinski, H.; Bebianno, M. J. Occurrence of Pharmaceutical Compounds and Pesticides in Aquatic Systems. *Mar. Pollut. Bull.* **2015**, 96, 384–400.
- (4) Miège, C.; Mazzella, N.; Allan, I.; Dulio, V.; Smedes, F.; Tixier, C.; Vermeirssen, E.; Brant, J.; O'Toole, S.; Budzinski, H.; Ghestem, J.-P.; Staub, P.-F.; Lardy-Fontan, S.; Gonzalez, J.-L.; Coquery, M.; Vrana, B. Position Paper on Passive Sampling Techniques for the Monitoring of Contaminants in the Aquatic Environment—Achievements to Date and Perspectives. *Trends Environ. Anal. Chem.* **2015**, 8, 20–26.
- (5) Poulter, G.; Lissalde, S.; Charriau, A.; Buzier, R.; Delmas, F.; Gery, K.; Moreira, A.; Guibaud, G.; Mazzella, N. Can POCIS be Used in Water Framework Directive (2000/60/EC) Monitoring Networks? A Study Focusing on Pesticides in a French Agricultural Watershed. *Sci. Total Environ.* **2014**, 497–498, 282–292.
- (6) Vrana, B.; Allan, I. J.; Greenwood, R.; Mills, G. A.; Dominiak, E.; Svensson, K.; Knutsson, J.; Morrison, G. Passive Sampling Techniques for Monitoring Pollutants in Water. *Trends Anal. Chem.* **2005**, 24, 845–868.
- (7) Huckins, J. N.; Petty, J. D.; Booij, K. Monitors of Organic Chemicals in the Environment. *Semipermeable Membrane Devices*; Springer: New York, 2006; pp 1–223.
- (8) Rusina, T. P.; Smedes, F.; Klanova, J.; Booij, K.; Holoubek, I. Polymer Selection for Passive Sampling: A Comparison of Critical Properties. *Chemosphere* **2007**, 68, 1344–1351.
- (9) Okay, O. Macroporous Copolymer Networks. *Prog. Polym. Sci.* **2000**, 25, 711–779.
- (10) *Macroporous Polymers: Production Properties and Biotechnological/Biomedical Applications*; Mattiasson, B., Kumar, A., Galeev, I. Y., Eds.; CRC Press, 2010; pp 1–513.
- (11) Han, J.; Du, G.; Gao, W.; Bai, H. An Anisotropically High Thermal Conductive Boron Nitride/Epoxy Composite Based on Nacre-Mimetic 3D Network. *Adv. Funct. Mater.* **2019**, 29, 1900412.
- (12) Chen, D.; Zhang, Y.; Ni, C.; Ma, C.; Yin, J.; Bai, H.; Luo, Y.; Huang, F.; Xie, T.; Zhao, Q. Drilling by Light: Ice-Templated Photo-Patterning Enabled by a Dynamically Crosslinked Hydrogel. *Mater. Horiz.* **2019**, 6, 1013–1019.
- (13) Leonhardt, E. E.; Kang, N.; Hamad, M. A.; Wooley, K. L.; Elsabahy, M. Absorbable Hemostatic Hydrogels Comprising Composites of Sacrificial Templates and Honeycomb-Like Nanofibrous Mats of Chitosan. *Nat. Commun.* **2019**, 10, 2307.
- (14) Lozinsky, V. I. Cryogels on the Basis of Natural and Synthetic Polymers: Preparation, Properties and Application. *Russ. Chem. Rev.* **2002**, 71, 489–511.
- (15) Okay, O.; Lozinsky, V. I. Synthesis and Structure–Property Relationships of Cryogels. *Polymeric Cryogels*; Advances in Polymer Science; Springer, 2014; Vol. 263, pp 103–157.
- (16) Lozinsky, V. I.; Okay, O. Basic Principles of Cryotropic Gelation. *Polymeric Cryogels*; Advances in Polymer Science; Springer, 2014; Vol. 263, pp 49–101.
- (17) Yang, M.; Wu, J.; Bai, H.; Xie, T.; Zhao, Q.; Wong, T.-W. Controlling Three-Dimensional Ice Template via Two-Dimensional Surface Wetting. *AIChE J.* **2016**, 62, 4186–4192.
- (18) Lozinsky, V. I.; Vainerman, E. S.; Korotaeva, G. F.; Rogozhin, S. V. Study of Cryostructurization of Polymer Systems III. Cryostructurization in Organic Media. *Colloid Polym. Sci.* **1984**, 262, 617–622.
- (19) Barrow, M.; Eltmimi, A.; Ahmed, A.; Myers, P.; Zhang, H. Frozen Polymerization for Aligned Porous Structures with Enhanced Mechanical Stability, Conductivity, and as Stationary Phase for HPLC. *J. Mater. Chem.* **2012**, 22, 11615–11620.
- (20) Ozmen, M. M.; Fu, Q.; Kim, J.; Qiao, G. G. A Rapid and Facile Preparation of Novel Macroporous Silicone-Based Cryogels via Photo-Induced Thiol–Ene Click Chemistry. *Chem. Commun.* **2015**, 51, 17479–17482.
- (21) Arrua, R. D.; Hilder, E. F. Highly Ordered Monolithic Structures by Directional Freezing and UV-Initiated Cryopolymerization. Evaluation as Stationary Phases in High Performance Liquid Chromatography. *RSC Adv.* **2015**, 5, 71131–71138.
- (22) Wong, T.-W.; Wu, J.; Yang, M.; Abdul Kadir, M. R.; Wahit, M. U.; Zhao, Q. Multifunctional Shape-Memory Foams with Highly Tunable Properties via Organo-Phase Cryopolymerization. *J. Mater. Chem. A* **2017**, 5, 9793–9800.
- (23) Akiba, M.; Hashim, A. S. Vulcanization and Crosslinking in Elastomers. *Prog. Polym. Sci.* **1997**, 22, 475–521.
- (24) Ceylan, D.; Okay, O. Macroporous Polyisobutylene Gels: A Novel Tough Organogel with Superfast Responsivity. *Macromolecules* **2007**, 40, 8742–8749.
- (25) Okay, O.; Durmaz, S.; Erman, B. Solution Crosslinked Poly(isobutylene) Gels: Synthesis and Swelling Behavior. *Macromolecules* **2000**, 33, 4822–4827.
- (26) Hu, Y.; Liu, X.; Zou, J.; Gu, T.; Chai, W.; Li, H. Graphite/Isobutylene-Isoprene Rubber Highly Porous Cryogels as New sorbents for Oil Spills and Organic Liquids. *ACS Appl. Mater. Interfaces* **2013**, 5, 7737–7742.
- (27) Ceylan, D.; Dogu, S.; Karacik, B.; Yakan, S. D.; Okay, O. S.; Okay, O. Evaluation of Butyl Rubber as Sorbent Material for the Removal of Oil and Polycyclic Aromatic Hydrocarbons from Seawater. *Environ. Sci. Technol.* **2009**, 43, 3846–3852.
- (28) Karakutuk, I.; Okay, O. Macroporous Rubber Gels as Reusable Sorbents for the Removal of Oil from Surface Waters. *React. Funct. Polym.* **2010**, 70, 585–595.
- (29) Su, E.; Okay, O. Cryogenic Formation-Structure-Property Relationships of Poly(2-acrylamido-2-methyl-1-propanesulfonic acid) Cryogels. *Polymer* **2019**, 178, 121603.

(30) Argun, A.; Can, V.; Altun, U.; Okay, O. Non-Ionic Double and Triple Network Hydrogels of High Mechanical Strength. *Macromolecules* **2014**, *47*, 6430–6440.

(31) Dogu, S.; Okay, O. Tough Organogels Based on Polyisobutylene with Aligned Porous Structures. *Polymer* **2008**, *49*, 4626–4634.

(32) Tuncaboylu, D. C.; Sahin, M.; Argun, A.; Oppermann, W.; Okay, O. Dynamics and Large Strain Behavior of Self-Healing Hydrogels with and without Surfactants. *Macromolecules* **2012**, *45*, 1991–2000.

(33) Tütem, E.; Apak, R.; Ünal, Ç. F. Adsorptive Removal of Chlorophenols from Water by Bituminous Shale. *Water Res.* **1998**, *32*, 2315–2324.

(34) Sarkar, M.; Acharya, P. K.; Bhattacharya, B. Modelling the Adsorption Kinetics of Some Priority Organic Pollutants in Water from Diffusion and Activation Energy Parameters. *J. Colloid Interface Sci.* **2003**, *266*, 28–32.

(35) Hill, A. V. The Combinations of Haemoglobin with Oxygen and with Carbon Monoxide. *Biochem. J.* **1913**, *7*, 471–480.

(36) Adibnia, V.; Hill, R. J. Universal Aspects of Hydrogel Gelation Kinetics, Percolation and Viscoelasticity from PA-Hydrogel Rheology. *J. Rheol.* **2016**, *60*, 541–548.

(37) Calvet, D.; Wong, J. Y.; Giasson, S. Rheological Monitoring of Polyacrylamide Gelation: Importance of Cross-Link Density and Temperature. *Macromolecules* **2004**, *37*, 7762–7771.

(38) Giraldo, J.; Vivas, N. M.; Vila, E.; Badia, A. Assessing the (a)symmetry of concentration-effect curves. *Pharmacol. Ther.* **2002**, *95*, 21–45.

(39) Tavsanlı, B.; Okay, O. Mechanically Robust and Stretchable Silk/Hyaluronic Acid Hydrogels. *Carbohydr. Polym.* **2019**, *208*, 413–420.

(40) Barton, A. F. M. *CRC Handbook of Solubility Parameters and Other Cohesion Parameters*, 2nd ed.; CRC Press: Boca Raton, Florida, 1991.